



Accurate relocation of seismicity along the North Aegean Trough and its relation to active tectonics



K.I. Konstantinou

Dept of Earth Sciences, National Central University, Jhongli 320, Taiwan

ARTICLE INFO

Keywords:
 Aegean
 Greece
 Seismicity
 Locking depth

ABSTRACT

The tectonics of northern Aegean are affected by the westward push of Anatolia and the gravitational spreading of the Aegean lithosphere that promote transtensional deformation in the area. This regime is also responsible for the creation of a series of pull-apart basins, collectively known as the North Aegean Trough. This work accurately relocates a total of 2300 earthquakes that were recorded along the North Aegean Trough during 2011–2016 by stations of the Hellenic Unified Seismic Network (HUSN) and strong-motion sensors. Absolute locations for these events were obtained using a nonlinear probabilistic algorithm and utilizing a minimum 1D velocity model with station corrections. The hypocentral depth distribution of these events shows a peak at 8 km diminishing gradually down to 20 km. A systematic overestimation of hypocentral depths is observed in the routine locations provided by the National Observatory of Athens where the majority of events appear to be deeper than 15 km. In order to obtain more accurate relative locations these events were relocated using the double-difference method. A total of 1693 events were finally relocated with horizontal and vertical uncertainties that do not exceed 0.11 km and 0.22 km respectively. Well-defined clusters of seismicity can be observed along the Saros and Sporades basins as well as the Kassandra and Sithonia peninsulas. These clusters either occur along the well-known NE-SW strike-slip faults bounding the basins, or along normal faults whose strike is perpendicular to the regional minimum stress axis. Locking depth along the North Aegean Trough is found to be remarkably stable between 13 and 17 km. This is likely a consequence of simultaneous reduction along the SW direction of heat flow (from 89 to 51 mW/m²) and strain rate (from 600 to 50 nstrain/yr) whose opposite effects are canceled out, precluding any sharp changes in locking depth.

1. Introduction

The tectonic setting of the eastern Mediterranean is shaped by the northward movement and subduction of the African lithosphere along the Hellenic arc at a rate of 0.9 cm/yr, as well as the westward movement of the Anatolian plate at a rate of 2.4–3.0 cm/yr (Fig. 1) (McClusky et al., 2000; Nyst and Thatcher, 2004; Hollenstein et al., 2008; Floyd et al., 2010; Reilinger et al., 2010). This movement of the Anatolian plate is accommodated by the dextral North Anatolian Fault which extends from the Karliova triple junction, traversing northern Turkey and the Marmara Sea before entering the northern Aegean. The area of the northern Aegean is strongly influenced by the strike-slip motion imposed by the Anatolian westward movement in addition to extension due to slab rollback and gravitational spreading of the Aegean lithosphere (Meijer and Wortel, 1997; Kiratzi, 2002; Konstantinou et al., 2016). This combination creates a transtensional tectonic regime as attested by a series of pull-apart sedimentary basins that extend from the Saros Gulf to the Sporades islands, collectively known as the North

Aegean Trough. These basins are bounded by NE-SW or ENE-WSW faults exhibiting predominantly shear as well as some extensional deformation (Koukouvelas and Aydın, 2002; Papanikolaou et al., 2002; McNeill et al., 2004; Ustaömer et al., 2008).

Several seismic reflection studies have been conducted in the northern Aegean with the aim of elucidating the shallow crustal structure of this area (Saatçılar et al., 1999; Laigle et al., 2000; McNeill et al., 2004; Ustaömer et al., 2008; Beniest et al., 2016 and references therein). These studies revealed that in the two largest basins (Saros and Sporades) the sedimentary layer thickness ranges from 1.5–3.5 km as a result of mass-wasting and landsliding near their margins. Except from the well-developed NE-SW faults, the reflection profiles also show the existence of E-W and NW-SE oriented faults which were interpreted as Riedel fractures resulting from the transtensional character of the stress field. On the other hand, the velocity field inferred from campaign and continuous GPS data suggests that there is a counter-clockwise rotation of Samothraki, Limnos and Agios Efstratios islands with differential motion that decreases from 20 mm/yr in Samothraki

E-mail address: kkonst@cc.ncu.edu.tw.

<http://dx.doi.org/10.1016/j.tecto.2017.08.021>

Received 13 April 2017; Received in revised form 16 August 2017; Accepted 17 August 2017

Available online 19 August 2017

0040-1951/ © 2017 Elsevier B.V. All rights reserved.

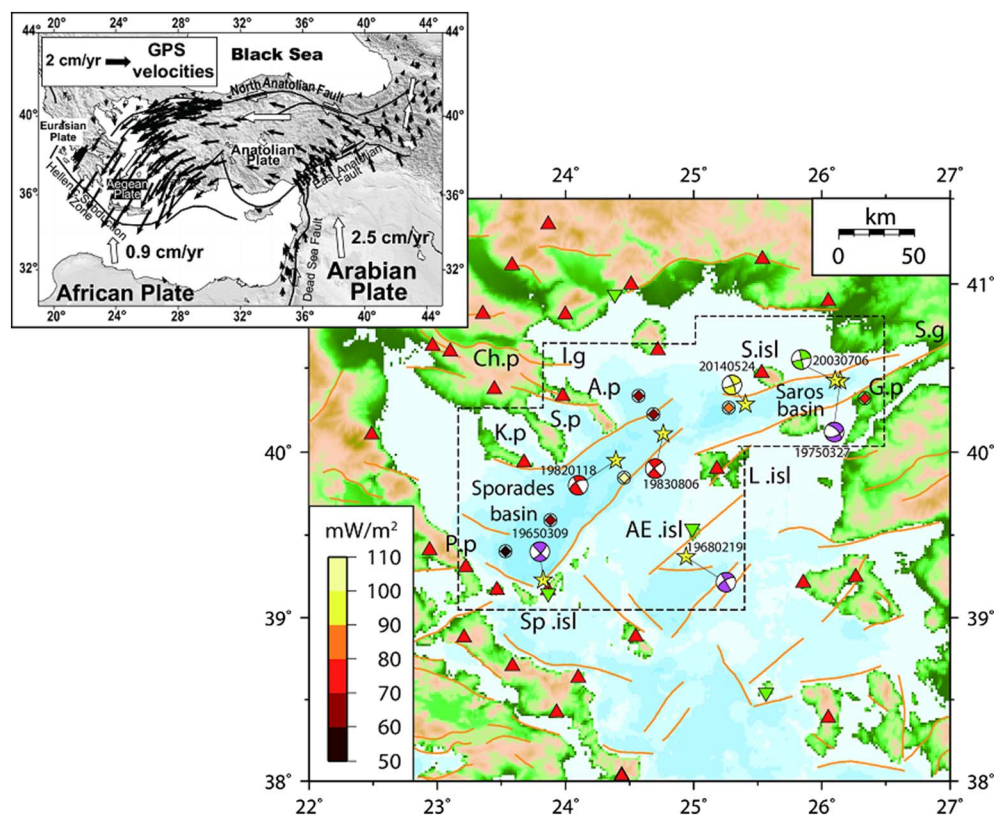


Fig. 1. Map showing the broader area of the northern and central Aegean. The dashed lines delineate the study area of the North Aegean Trough. Darker blue color indicates deeper points in the bathymetry. Solid orange lines indicate traces of active faults contained in the GREDASS database (Caputo and Pavlides, 2013). The yellow stars represent large earthquakes that have occurred in the area surrounded by dashed lines from 1965 until now. Purple beachballs were taken from Taymaz et al. (1991), red beachballs are solutions from Global CMT, the green beachball was adopted from Karabulut et al. (2006) and the yellow one from NOA, Institute of Geodynamics moment tensor database. Red triangles represent HUSN stations while inverted green triangles are the strong-motion stations utilized in this study. Diamonds within a circle depict heat flow measurements taken from Jongsma (1974) and Pfister et al. (1998) corresponding to a color that varies according to the scale shown in lower left hand corner. Sp.isl: Sporades islands, P.p: Pilion peninsula, Ch.p: Chalkidiki peninsula, K.p: Kassandra peninsula, S.p: Sithonia peninsula, A.p: Athos peninsula, I.g: Ierissos Gulf, S.isl: Samothraki island, L.isl: Limnos island, AE.isl: Agios Efstratios island, S.g: Saros Gulf, G.p: Gelibolu peninsula. The inset map at the top left hand corner shows the geodynamic setting in the eastern Mediterranean along with the GPS velocity field (after Reilinger et al., 2010). (For interpretation of the references to color in this figure legend, the reader is referred to the web version of this article.)

to 7 mm/yr in the Sporades basin (Müller et al., 2013). This decreasing trend from NE to SW is also mirrored by shear strain rates that attain values between 400 and 600 nstrain/yr at Saros and Samothraki, progressively diminishing to about 50 nstrain/yr or less in the Sporades islands (Kreemer et al., 2004; Müller et al., 2013).

The area of the northern Aegean has a rich record of historical seismicity as demonstrated by several destructive earthquakes with magnitudes between 6 and 7.5 having occurred over the last few hundred years (Papazachos and Papazachou, 2003). During the last 50 years several large (M_s or $M_w > 5.5$) earthquakes occurred that confirmed the dominance of strike-slip faulting in this area (Table 1 and Fig. 1). All of these events nucleated along the NE-SW faults that propagate from the Saros Gulf to the Sporades basin, except from the 1968 event that ruptured a similarly oriented fault segment whose trace traverses the small island of Agios Efstratios (Pavlides and Tranos, 1991). The latest large earthquake to occur in the North Aegean Trough was the 24 May 2014 ($M_w \sim 6.8$) Samothraki earthquake. This event exhibited a number of peculiar characteristics such as the lack of large aftershocks, reduced levels of ground shaking and a super-shear rupture

Table 1

List of source parameters for large earthquakes (M_s or $M_w > 5.5$) that have occurred within the study area during the last 50 years. H signifies hypocentral depth while the letter ‘f’ next to the depth value means that hypocenter was fixed during the location. EHB refers to the global relocation catalog of Engdahl et al. (1998). Focal mechanisms of these events are shown in Fig. 1.

| Date | Time | Lat | Lon | H (km) | M_s | M_w | Reference |
|----------|----------|--------|--------|--------|-------|-------|-------------------------|
| 19650309 | 17:57:53 | 39.229 | 23.826 | 4.8 | 6.1 | – | EHB |
| 19680219 | 22:45:43 | 39.369 | 24.942 | 8.9 | 7.1 | – | EHB |
| 19750327 | 05:15:07 | 40.424 | 26.143 | 3.3 | 6.6 | – | EHB |
| 19820118 | 19:27:27 | 39.949 | 24.392 | 15f | 6.9 | 6.6 | EHB |
| 19830806 | 15:43:54 | 40.107 | 24.762 | 10f | 6.9 | 6.7 | EHB |
| 20030706 | 19:10:28 | 40.427 | 24.762 | 18 | – | 5.7 | Karabulut et al. (2006) |
| 20140524 | 09:25:01 | 40.285 | 25.403 | 28 | – | 6.8 | NOA |

speed (Evangelidis, 2015; Saltogianni et al., 2015; Kiratzi et al., 2016). The installation and continual upgrade of regional seismic networks improved considerably the monitoring capabilities in this area, however, available routine locations still lack the resolution needed in order to be utilized effectively for detailed studies of active tectonics. This is particularly true when the aim is to investigate hypocentral depth variations and their relationship with heat flow, which in turn influences the seismogenic layer thickness and the resulting seismic hazard.

In this work the seismicity distribution along the North Aegean Trough is studied during the period 2011–2016. Focusing on this period is justified not only because it includes the seismicity prior to and after the 2014 Samothraki earthquake, but also because the high-quality data recorded by a large number of permanent seismic stations allow one to obtain much more accurate event locations compared to all previous periods. First, absolute locations of all events are obtained by utilizing a probabilistic nonlinear location algorithm and by employing a minimum 1D velocity model. This is followed by a comparison of these locations with routine locations provided by the National Observatory of Athens (NOA), Institute of Geodynamics, which is the agency responsible for the seismic monitoring of the Greek region. Accurate relative locations are then derived and the resulting seismicity distribution is interpreted in terms of regional tectonics and the prevailing crustal stress field. The depth distribution of the relocated events is used to infer fault locking depth, whose relationship with heat flow values is discussed.

2. Data

The seismic activity in the Aegean Sea is monitored by four permanent seismic networks, where the three of them are operated by Greek Universities (Athens, Thessaloniki, Patras) while the fourth is operated by NOA, Institute of Geodynamics. In 2008 these four networks merged into one network which was named Hellenic Unified Seismic Network (HUSN) and since then all recorded data are sent to NOA where routine processing and determination of earthquake source

parameters takes place. HUSN consists of 120 stations that are equipped with three-component seismometers representing a mixture of sensor types (CMG-40 T, CMG-3ESP, Lennartz Le-3D, STS-1, STS-2, Trillium 120P). This network covers most of Greece and specifically for the northern Aegean its coverage can be considered quite satisfactory with a good azimuthal distribution around the North Aegean Trough (cf. Fig. 1). In addition to HUSN stations, several strong-motion sensors are installed in the nearby islands and their data can also be used increasing the number of available stations to 32 and improving azimuthal coverage. HUSN had undergone several upgrades in the period 2008–2011, therefore this study focuses on data recorded from early 2011 until the end of 2016 when both data quality and quantity was the highest. The NOA catalog was searched in order to extract earthquake data for the areas enclosed within the dashed lines in Fig. 1, effectively encompassing the North Aegean Trough and its adjacent islands of Limnos, Agios Efstratios as well as the three peninsulas of Chalkidiki (Kassandra, Sithonia, Athos). This search yielded a total of 2300 earthquakes, the majority of them recorded by 8 stations or more. These were manually picked by NOA staff and for every phase pick a weight factor was also assigned with ‘0’ weight signifying the best quality pick and ‘4’ the worst. Most of the P-phase picks had a weight of 0 while the S-phase picks had weights between 1 and 2. The majority of the earthquakes during the period of study had local magnitudes smaller than 3.0, however, two events near Sithonia peninsula had moment magnitudes of 5.1–5.2 and the 24 May 2014 earthquake near Samothraki had a moment magnitude of 6.8 ($M_L = 6.3$) as determined by NOA.

3. Absolute locations

3.1. Methodology and results

In the past earthquake locations were usually obtained by applying different versions of the method proposed by Geiger (1912) that represent linearized approximations to the actual nonlinear problem. The significant improvement in computer power and speed during the last decade has allowed the application of algorithms that solve the nonlinear location problem without resorting to any such approximation. The basic concept of these algorithms is that the determination of an earthquake location can be done by a set of points sampled from the posterior probability density function (PDF) (Tarantola and Valette, 1982; Moser et al., 1992; Lomax et al., 2000). The number and quality of the picked phases, as well as the station distribution around the event have a strong influence on the shape and volume of the PDF. This means that the sampled PDF can then be used for assessing the accuracy of the earthquake location since small volume, quasi-ellipsoidal PDFs signify well-constrained locations. In this study, the software package NLLOC (freely available at www.alomax.free.fr/nlloc last accessed 16 June 2017) is used in order to obtain nonlinear probabilistic locations for the earthquakes along the North Aegean Trough. NLLOC estimates optimal earthquake locations by finding the maximum likelihood of the nonlinear location of the PDF, utilizing the Oct-tree search algorithm (for an overview see Lomax et al., 2009). NLLOC also allows the usage in the location problem of the Equal Differential-Time (EDT) function (e.g. Font et al., 2004) which is an objective function formed from the differences between the residuals of one event recorded at a pair of stations. The combination of EDT with the PDF has been found to produce robust locations even when large outliers are present.

NLLOC requires that theoretical travel times are pre-calculated along a 3D grid, whose dimensions in this case were chosen as $500 \times 500 \times 180$ cells with node spacing of $1 \times 1 \times 1$ km. This calculation was performed by using the finite difference algorithm of Podvin and Lecomte (1991) and utilizing the minimum 1D velocity model of Karabulut et al. (2006) (hereafter called K06 model) (Table 2). The K06 model was derived from inversion of travel times of aftershocks that occurred after the 2003 Saros Gulf earthquake, providing good raypath coverage over the northern Aegean. As the K06 model

Table 2

P-wave velocity model of Karabulut et al. (2006) that is used for obtaining absolute and relative locations of the earthquakes studied in this paper. The velocity of the last depth entry is assumed to continue downwards as a halfspace.

| Depth (km) | Vp (km/s) |
|------------|-----------|
| 0.0 | 2.90 |
| 2.5 | 3.80 |
| 4.0 | 5.20 |
| 6.0 | 5.90 |
| 12.5 | 6.25 |
| 14.0 | 6.50 |
| 18.0 | 6.70 |
| 22.5 | 7.00 |
| 26.0 | 7.20 |
| 31.0 | 7.60 |
| 35.0 | 7.75 |
| 37.0 | 7.90 |
| 42.0 | 8.10 |

included only P-wave velocities, the corresponding S-wave velocities were obtained by using a mean V_p/V_s ratio of 1.73 estimated from Wadati diagrams. Stations that were located further inside the Greek mainland were excluded from the location process for the reason that the K06 model would become more inaccurate away from the northern Aegean. The earthquake location using NLLOC was then performed in two steps: at first initial locations were obtained and mean residuals were calculated for each station and each phase (P and S) with the aim of using them as station delays. These station delays were then used as correction factors for the arrival times of each event and the location process ran for a second time in order to estimate final absolute locations. Horizontal and vertical uncertainties for each location were estimated by using the diagonal elements of the covariance matrix which depend on the exact shape of the PDF, thus for an irregular PDF these would be larger (Maleki et al., 2013).

Fig. 2 shows the locations estimated by NLLOC using the K06 velocity model and station corrections, along with the spatial variation of the horizontal (ERH) and vertical (ERV) uncertainties. It can be seen that the largest horizontal uncertainties (> 4 km) are observed for events located in the Saros Gulf and Gelibolu peninsula which are areas at the edge or outside HUSN. The remaining events have horizontal uncertainties of 3 km or smaller while the mean horizontal uncertainty for all events is 3.2 km. Vertical uncertainties also seem to be larger than 4 km in Saros and Gelibolu, as well as for events located in the area between Limnos and Sporades islands. On the other hand, events that are located near a recording station tend to have smaller (< 4 km) vertical uncertainty that is closer to the mean value for all events, which is 3.9 km. The epicenter of the 2014 Samothraki earthquake was located at latitude 40.3049° , longitude 25.3789° with a hypocentral depth of 12.9 km (± 1.5 km). The distribution of seismicity exhibits significant clustering of events along the fault that borders the northern edge of the Saros basin, along Sithonia and Kassandra peninsulas, and the Sporades basin. It is also interesting to note the lack of significant seismicity along the fault that borders the Sporades basin in the area between Limnos and Sporades (cf. Fig. 2).

3.2. Comparison with NOA routine locations

An important question is how much improved are the probabilistic nonlinear locations when compared to the routine locations provided by NOA. The RMS residual and the hypocentral depth are the two most suitable quantities for comparison (Fig. 3); this is because the first one reflects the quality of the location and the suitability of the velocity model used, while the second represents a parameter that is usually the most difficult to constrain in location problems. The NOA RMS residual is spread from 0.2 to 0.7 s with a mean value of 0.4 s and a standard

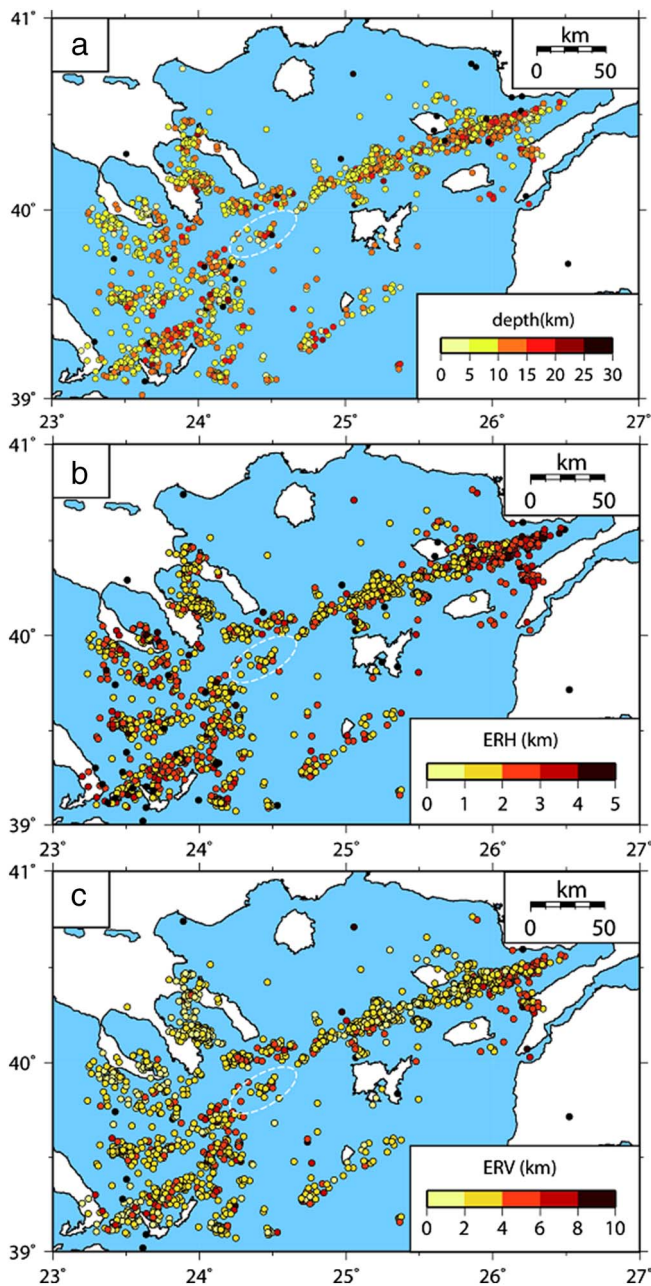


Fig. 2. Maps showing absolute locations obtain from NLLOC as a function of (a) hypocentral depth, (b) horizontal uncertainty ERH, (c) vertical uncertainty ERV. The dashed ellipse highlights the part of the North Aegean Trough that exhibits little seismicity.

deviation of 0.1 s. On the other hand, the locations obtained by NLLOC exhibit a reduced residual spread from 0.2 to 0.5 s with a mean value of 0.3 s and a standard deviation of 0.07 s. The distribution of hypocentral depths is distinctly different, with NOA depths exhibiting a small peak at 15 km and a much larger one at 28 km while many events have depths between these two values. On the contrary, NLLOC depths exhibit a single peak at 8 km followed by a progressive diminishing in the number of deeper events down to about 20 km. Taking into account that the Moho depth in the northern Aegean is rather flat and between 25 and 28 km (Soudoudi et al., 2006), the second peak in NOA depths seems physically unrealistic. NOA is also routinely inverting HUSN waveforms for the purpose of determining moment tensors of larger events ($M_L > 3.0$). This process inverts the waveforms at different depths and then selects the best solution based on which depth minimizes misfit, or maximizes the variance reduction between observed

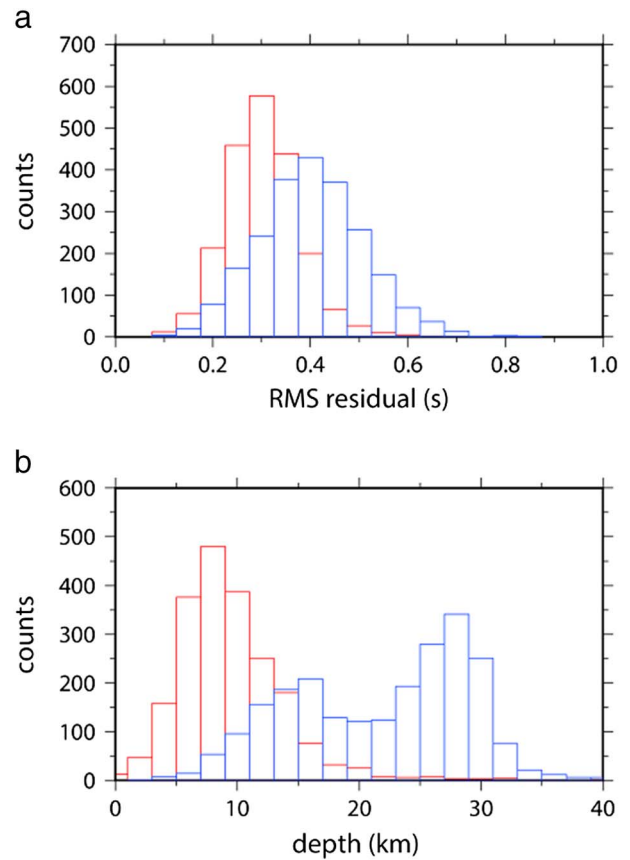


Fig. 3. Comparison between NLLOC locations and NOA routine locations: (a) histogram showing the distribution of RMS residual for NLLOC locations (red bars) and NOA routine locations (blue bars), and (b) histogram showing the distribution of hypocentral depths; symbols are the same as in (a). (For interpretation of the references to color in this figure legend, the reader is referred to the web version of this article.)

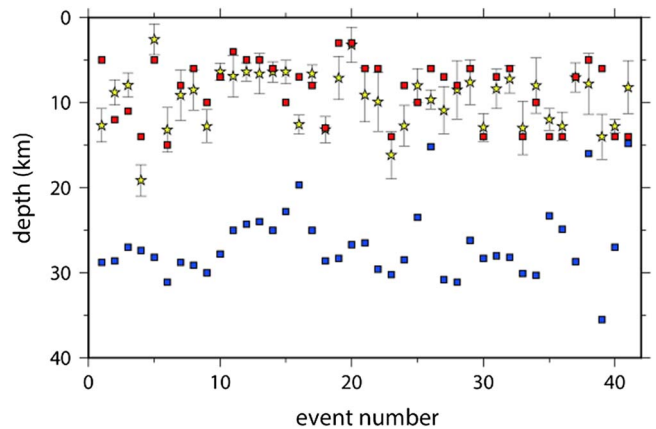


Fig. 4. Diagram showing the comparison between different estimates of hypocentral depth for 42 events that occurred in the study area. Yellow stars represent NLLOC hypocentral depths and error bars depict vertical uncertainties. Red squares are depths obtained after waveform inversion for the determination of the moment tensor. Blue squares are routine hypocenters determined by NOA. (For interpretation of the references to color in this figure legend, the reader is referred to the web version of this article.)

and synthetic waveforms (Konstantinou et al., 2010). Since inversions are performed every 1–2 km, it is possible to compare NOA and NLLOC hypocenters with these depths. A comparison for 42 events that have moment tensor solutions, suggests a good agreement between depths determined by NLLOC and depths obtained from moment tensor inversion (Fig. 4). This comparison also highlights that the difference between hypocenters determined by NOA and the other two estimates

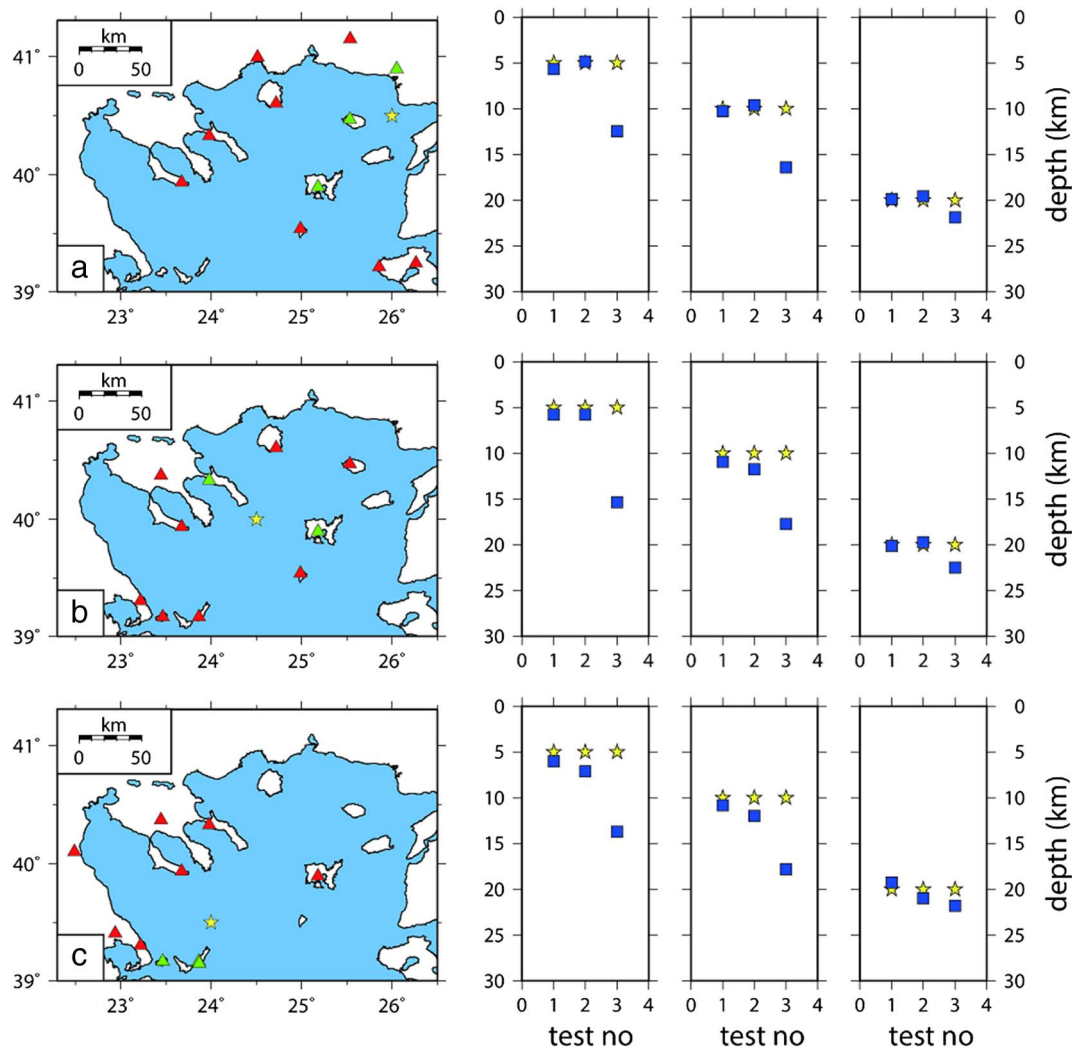


Fig. 5. Summary of the synthetic location tests described in the text. Each map shows the stations used in the test (triangles) and the assumed event location (star). Stations shown as green triangles are assumed to have both P- and S-phase picks, while red triangles are stations with only P-phases. Each diagram shows the number of each test (1, 2, or 3), the true depth (star) and the hypocentral depth obtained after inversion of the synthetic arrival times (blue squares). (For interpretation of the references to color in this figure legend, the reader is referred to the web version of this article.)

is in the order of 10 km or more.

The comparison of NOA hypocentral depths with those obtained by NLLOC showed significant differences despite the fact that the same picks were used in both cases. In order to understand better the causes of this difference, synthetic tests were conducted by assuming three fictitious events at different locations along the North Aegean Trough (Fig. 5). It was further assumed that these events were recorded by only 8 stations and that the two closest stations also recorded an S-phase. Hypocentral depths of 5, 10, 20 km were assigned to each of these events and synthetic arrival times were calculated using the algorithm of Podvin and Lecomte (1991) utilizing the K06 velocity model. Three test locations were performed where during test 1 only the network geometry was considered as a factor. In test 2 the synthetic arrivals times were randomized with the addition of Gaussian noise having zero mean and a variance of 0.05 s for P-phases and 0.1 s for S-phases, as a means of replicating picking errors. Finally, in test 3 in addition to network geometry and picking errors, the effect of the velocity model was also added: the velocity model used to locate the events changed from K06 to a much simpler one consisting of two layers and a half-space (layer 1: 19 km, 6.0 km/s; layer 2: 12 km, 6.6 km/s; half-space velocity: 7.9 km/s; $V_p/V_s = 1.73$) as the one used by NOA. Synthetic arrival times were inverted using NLLOC and during all these tests the epicentral locations were recovered with shifts in the order of 100 m

from the true location. If only station coverage and picking errors are considered, the hypocentral depths could also be recovered with shifts of < 2 km from the true depth. However, depth accuracy suffers considerably when a simpler model is used for locating shallow events at depths of 5 and 10 km with shifts ranging from 7 to 10 km from the true depth (cf. Fig. 5). On the contrary, events with depths of 20 km were always located near the true depth with shifts of about 2 km. These results partly explain the occurrence in NOA locations of a significant number of events in the lower crust (15–20 km), even though the cause for the mislocation of events in the upper mantle (> 25 km) remains unclear and may also be connected to re-weighting practices by NOA staff as a way of minimizing residuals at particular stations.

4. Relative locations

4.1. Methodology and error analysis

For the purpose of enhancing the accuracy of locations obtained with NLLOC, relative locations were calculated using the double-difference algorithm (hereafter called HYPODD) of Waldhauser and Ellsworth (2000). The basis of this algorithm stems from the idea that when the distance between the hypocenters of two events is much smaller than their distance to the recording station, then the spatial

offset of these two events controls their travel time difference at that station. HYPODD considers pairs of earthquakes recorded at common stations and minimizes in an iterative way their observed and theoretical travel times by adjusting the difference in their hypocentral location distance. The algorithm makes use of differential travel times calculated from catalog data and/or from waveform cross-correlation of P-/S-waves. To date HYPODD has been extensively used in order to obtain accurate relative locations as a means of imaging fault structures in several areas around the world.

Prior to the application of HYPODD differential travel times were calculated using NLLOC catalog locations, by applying a separation distance of 10 km for stations located up to 300 km away from the sources. Each event was required to be connected with 10 other neighboring events in order to improve connectivity. The neighboring events are considered strong links only in the case when each link includes at least eight phase pairs as suggested by Waldhauser (2001). A total of 2055 events conformed with these requirements, creating a network of links that consisted of 114,532 P-phase and 58,719 S-phase pairs. The calculation of differential travel times also yielded the average number of links per event pair and the average offset of strongly linked events which in this case were 14 events and 3.5 km respectively. The percentage of outliers and weakly linked events was 3% and 15% respectively, signifying the high quality and tight clustering for the majority of the data.

The relocation of the events was performed by using the LSQR conjugate gradients method that solves the damped least-squares problem and is suitable for large datasets. The damping parameter was chosen equal to 50 as this value produced condition numbers that were between 40 and 80 for the majority of the clusters (see Waldhauser, 2001). The a priori weights that were applied to the data were 1.0 for the P-wave and 0.5 for the S-wave observations while after the first 6 iterations larger weights were assigned to small inter-event distances for both P- and S-wave observations (e.g. Roumelioti et al., 2003). The velocity model K06 with a V_p/V_s ratio of 1.73 was again utilized in order to compute theoretical differential travel times. From the original 2055 events HYPODD finally relocated 1693 events (~82%) due to the loss of link between events during the iterative relocation process. The mean value of the RMS residual after the relocation became 0.12 s exhibiting a significant reduction when compared to the mean RMS residual of NLLOC locations (~0.3 s). Despite its efficiency in solving large problems, the LSQR method does not provide reliable estimates of the horizontal and vertical uncertainties for the relocated events. In order to properly assess these uncertainties four smaller clusters were relocated using the Singular Value Decomposition (SVD) method. Table 3 gives detailed information about these clusters and also includes the average uncertainties of the relocated events in each cluster. As it can be seen average horizontal uncertainties do not exceed 0.11 km, while average vertical uncertainties attain a maximum value of 0.22 km.

4.2. Results

Fig. 6 shows a map of the relative locations superimposed on the traces of known active faults in the North Aegean contained in the

Table 3

Details of the clusters relocated using SVD in order to assess relocation uncertainties. Neq is the number of earthquakes contained in each cluster, cLat cLon cH represent the cluster centroid location and depth, and ErrX ErrY ErrZ are the corresponding mean uncertainties.

| ID | Neq | cLat | cLon | cH (km) | ErrX (km) | ErrY (km) | ErrZ (km) |
|----|-----|---------|---------|---------|-----------|-----------|-----------|
| 1 | 220 | 40.2157 | 25.1625 | 8.6 | 0.05 | 0.04 | 0.11 |
| 2 | 88 | 40.0206 | 24.2772 | 9.5 | 0.08 | 0.08 | 0.22 |
| 3 | 64 | 39.5316 | 23.4926 | 7.6 | 0.11 | 0.06 | 0.19 |
| 4 | 48 | 39.9266 | 23.4242 | 8.0 | 0.10 | 0.08 | 0.20 |

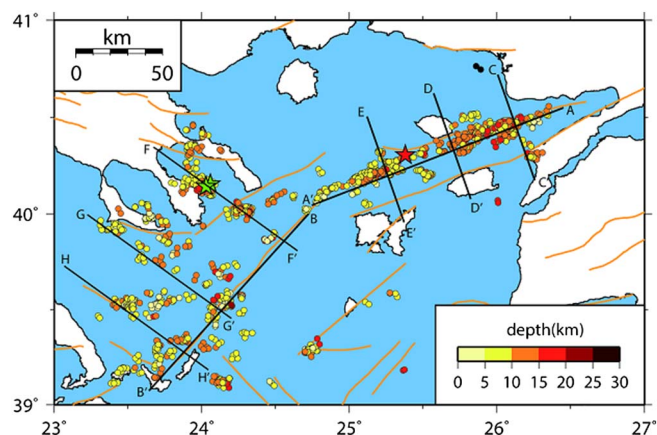


Fig. 6. Map showing results obtained after relocation with HYPODD. The color of each circle corresponds to a depth value according to the scale at the lower right hand corner. The red star is the NLLOC location of the 24 May 2014 (Mw 6.8) earthquake (see text for more details). The two green stars represent the locations of the two moderate events at Sithonia peninsula. Orange solid lines represent active fault adopted from the GREDASS database (Caputo and Pavlides, 2013). Black solid lines are depth cross-sections shown in later Figures. (For interpretation of the references to color in this figure legend, the reader is referred to the web version of this article.)

GREDASS database (Caputo and Pavlides, 2013). It should be noted that the hypocenter of the 24 May 2014 earthquake was not relocated by HYPODD, most likely because there were very few nearby events resulting in a loss of links; instead the NLLOC location is being plotted on the map and on the depth cross-sections. Along the Saros basin seismicity is focused on the northern bounding fault, exhibiting an initial widening of its surface expression and then a progressive narrowing towards SW. Smaller elongated clusters of events appear on either side of the main fault most notably near Gelibolu peninsula, to the east of Samothraki, and to the south of the 2014 earthquake. Depth cross-sections across the main fault reveal a rather steep distribution of hypocenters, where at shallow depths it looks more diffuse becoming narrower at greater depth (Fig. 7). These hypocenter distributions seem to agree well with numerical simulations of damage distribution in strike-slip faults where the damage zone is broader near the surface and becomes very localized at depth (Finzi et al., 2009). The cross-section along the axis of the fault zone shows that near Saros Gulf seismicity extends to a considerable range of depths (3–20 km) in accordance with the previous results of Karabulut et al. (2006). To the SW of Samothraki relocated hypocenters tend to cluster within a narrow depth interval (7–12 km), leaving an area almost free of any earthquakes. In fact this area represents one of the two slip patches that ruptured during the 2014 earthquake as derived by Kiratzi et al. (2016) after inverting teleseismic waveforms (cf. Fig. 7). The other slip patch appears to extend below the brittle-ductile boundary, reaching very close to the Moho (~27 km). Even though this feature is unusual Kiratzi et al. (2016) state that it is not an artifact, as it is required if one wants to obtain a good fit between observed and synthetic waveforms. Obviously, this issue can be resolved only after inversion of regional weak and strong-motion waveforms in order to better constrain the slip distribution. In the remaining part of the cross-section the hypocenters move from 15 km to shallower than 10 km and are also looking more diffuse.

Along the basin that extends from the tip of Athos peninsula to the Sporades islands the seismicity shows well-defined clusters which however, do not always coincide with known active faults (cf. Fig. 6). The most prominent example of this is the large cluster in Sithonia peninsula that also includes the aftershocks of two moderate earthquakes (Mw ~5.1–5.2) that occurred in 14 February and 4 March 2012 and corresponded to normal faulting events. This cluster seems to define a fault with a length of 25 km that is almost parallel to the faults

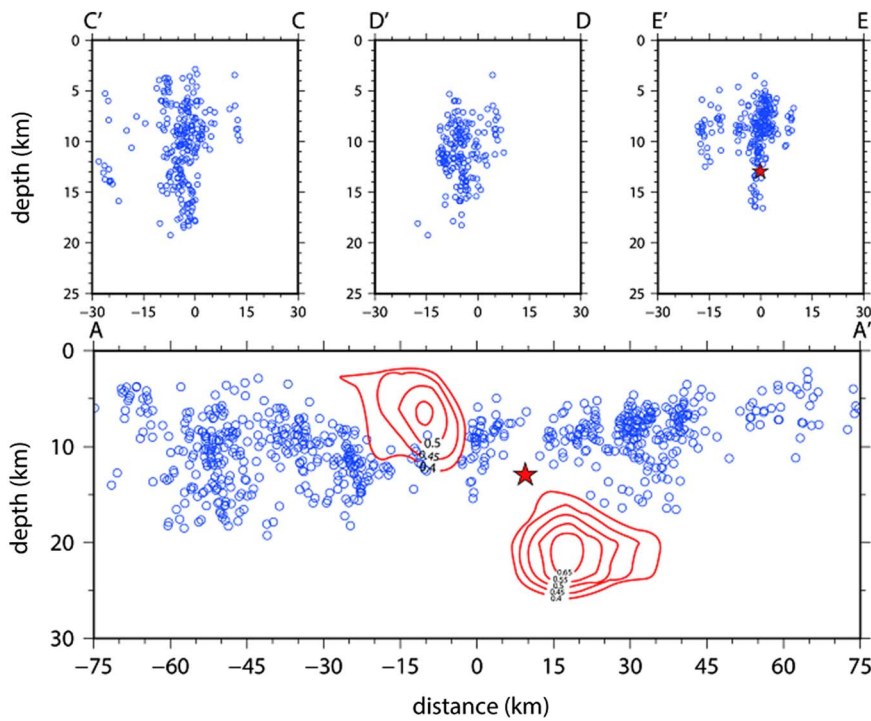


Fig. 7. Depth cross-sections corresponding to the profiles defined in Fig. 6. The red star represents the hypocenter of the 24 May 2014 earthquake. The red curves represent the two slip patches derived by Kiratzi et al. (2016) for this event after inversion of teleseismic waveforms. The unit of the slip contours is meters. (For interpretation of the references to color in this figure legend, the reader is referred to the web version of this article.)

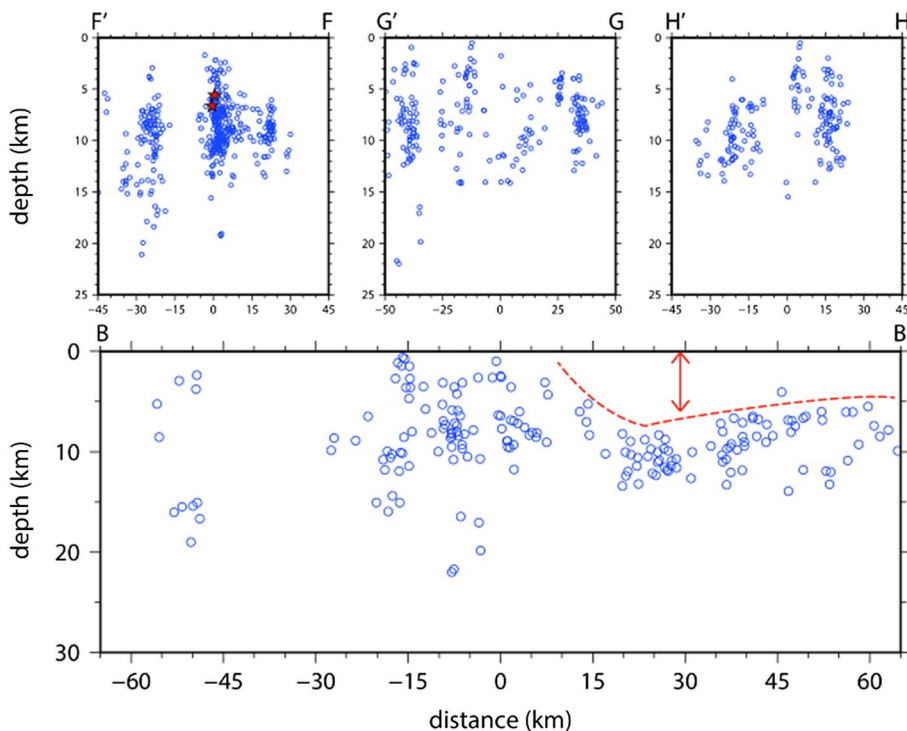


Fig. 8. Same as in Fig. 7 for the rest of the depth cross-sections. The red dashed curve roughly coincides with the outline of the crystalline basement of the Sporades sedimentary basin. The double arrow marks the deeper point of the basin and the thickest accumulation of sediments according to Beniast et al. (2016). The two red stars represent the hypocenters of the moderate events in Sithonia peninsula. (For interpretation of the references to color in this figure legend, the reader is referred to the web version of this article.)

that traverse Ierissos Gulf and Athos peninsula. The cross-section F-F' depicts the hypocenters of the two largest earthquakes at 5–6 km depth, while all other events extend from 2 km down to about 14 km (cf. Fig. 8). The geometrical characteristics of this fault imply a rupture area of 300 km². Konstantinou (2014) derived the relationship $M = (4/3) \log A + 3.07$ (when $A > 251 \text{ km}^2$) for the Mediterranean region in order to estimate the moment magnitude M of an earthquake generated by a fault when the rupture area A of this fault is known. Based on this relationship, if the fault near Sithonia ruptures during a single earthquake, the moment magnitude of such an event will be equal to 6.3. The

close proximity of this fault to densely populated areas in Chalkidiki warrants further investigation into its seismogenic potential by future studies.

Cross-section G-G' shows a rather diffuse image of the seismicity between Kassandra and Sporades that is distributed from a few kilometers from the surface down to 15 km depth (Fig. 8). A well-defined cluster is located to the east of Pilion peninsula, at the edge of an active fault imaged previously by Laigle et al. (2000). Cross-section H-H' shows seismicity extending from the surface down to 13 km, later becoming restricted to depths 5–15 km within the Sporades basin. Little

seismicity is observed along the first 50 km of the NE-SW fault that extends towards the Sporades islands (cf. Fig. 2). Further to the SW a large cluster is located close to Sporades islands and other smaller clusters can be found within the Sporades basin. Cross-section B-B' along the whole length of this fault reveals that shallow (< 5 km) seismicity vanishes beneath the Sporades basin, becoming shallower again further SW. This depth distribution agrees well with the bathymetry of the basin and the thickness of the deposited sediments which at the deepest (~ 1.6 km) point of the basin attains a value of 3.5 km (Beniest et al., 2016).

5. Discussion

5.1. Seismicity and crustal stress field

As mentioned earlier the North Aegean Trough represents an area that is affected by deformation due to the combined influence of the westward escape of Anatolia and the gravitational spreading of the Aegean lithosphere. Recently, Konstantinou et al. (2016) inverted a large number of earthquake focal mechanisms in order to obtain stress axes orientations along a regular grid of nodes with spacing of 0.35° for the whole of Greece. The resulting stress field exhibited those spatial variations that were strongly required by the data, since the stress inversion minimized any difference between each node and adjacent nodes. For all nodes in the northern Aegean the orientations of the maximum and minimum stress axes were found very close to horizontal (plunge 4° – 12°), while the azimuth of the maximum stress axis varied by a few degrees around $N283^\circ E$ and of the minimum stress axis around $N15^\circ E$. Uncertainties were estimated using bootstrap resampling and were found to be 10° or less for both azimuth and plunge of the principal stress axes.

Fig. 9 shows a cartoon illustrating the principal stress axes configuration along the North Aegean Trough relative to the orientation of known faults as well as hypothesized faults that correspond to earthquake clusters. The main NE-SW fault that traverses the Saros basin exhibits a dextral strike-slip motion as demonstrated by the focal mechanisms of the 2003 and 2014 earthquakes (cf. Fig. 1). It is also optimally oriented for failure with respect to the maximum stress axis,

since the reactivation angle θ_1 has a value of about 33° . The NW-SE oriented fault that is depicted to the south of the main shear zone has been inferred from the cluster of events elongated in this direction and seems to coincide with a fault imaged by McNeill et al. (2004) which separates the Saros basin into eastern and western sub-basins. McNeill et al. (2004) suggested that this fault may be a sinistral strike-slip fault based on seafloor imaging observations of left-lateral displacement of slump debris. The two other hypothesized faults, the one north of the main shear zone and the other near Gelibolu peninsula have no kinematic indicators, however, the first is almost perpendicular to the minimum stress axis and the second has an oblique orientation. It is therefore likely that the first is a small normal fault and the second exhibits strike-slip with some normal component of motion.

The NE-SW fault that extends from Limnos island to the Sporades basin forms an angle θ_2 equal to 66° with the maximum stress axis, suggesting a severe misorientation with respect to the prevailing stress field (Sibson, 1990). This is similar to estimates of the reactivation angle for the 1965 and 1983 earthquakes (62° and 57° respectively) that presumably occurred along this fault. On the contrary, the 1982 earthquake that is located further away from this fault shows a smaller reactivation angle of 45° . Even though the accuracy of this location is not high, taking into account the transtensional tectonics of this area leads to the speculation that this earthquake might have occurred at a different fault which may represent an R Riedel fracture relative to the main shear zone. It is beyond the scope of this work to investigate the mechanics of reactivation for this severely misoriented fault, however, low coefficient of friction and/or high fluid pressure in the fault core are two commonly cited mechanisms (see for example Tembe et al., 2009). Fig. 9 also includes faults A and B that exhibited substantial seismicity during the study period. Fault A corresponds to the normal fault imaged by Laigle et al. (2000), while fault B runs almost parallel to the coast of Sithonia peninsula and is also normal as indicated by the focal mechanisms of the two largest earthquakes. Both faults form a large angle with the direction of the minimum stress axis, confirming the field observations of Chatzipetros et al. (2013) on the islands of the north Aegean about the co-existence of main shear zones and smaller normal faults.

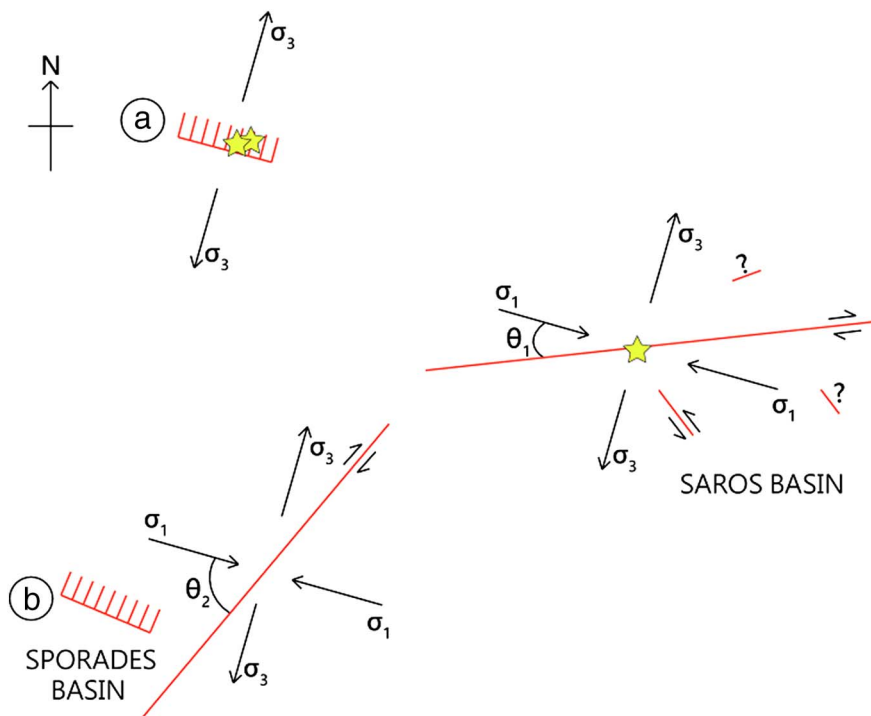


Fig. 9. Cartoon illustrating the configuration of the principal stress axes determined by Konstantinou et al. (2016) and the orientation of main fault zones in the study area. The yellow stars represent locations of moderate/large events. Comb-like lines represent normal faults (see text for more details). Note that the length of the lines are not scaled based on the actual fault lengths. (For interpretation of the references to color in this figure legend, the reader is referred to the web version of this article.)

5.2. Locking depth and thermal conditions

The locking depth of a strike-slip fault can be defined as the depth that separates the brittle part of the crust where seismicity occurs, from the deeper ductile part that slips freely without producing any earthquakes (Vernant, 2015). There are two ways to infer locking depth, either from seismic observations of hypocentral depth distribution or from geodetic observations in the form of GPS velocities. In the North Aegean Trough Müller et al. (2013) determined geodetic locking depth along three profiles that were close to C-C', D-D' and H-H' profiles shown previously in Fig. 6. Seismic locking depth was then estimated as the depth value corresponding to the 95th percentile of the depth distribution for events along these profiles as well as profile E-E'. For profiles C-C', D-D' and E-E' this estimation was performed using all the events as well as only the events that occurred before the Samothraki earthquake. It was found that the locking depth estimated in either way was almost the same, which implies that seismicity was occurring at the same depths before and after this large event.

Except from determining seismic locking depth, geotherms were also calculated for the purpose of investigating the effect of temperature on the thickness of the seismogenic layer. Calculations were performed by using the 1D steady-state heat conduction equation and utilizing the heat flow values closer to each profile (cf. Figs. 1 and 6). The upper crust was assumed to consist of wet quartzite while the lower crust was considered to be made of diabase. Table 4 gives a summary of thermal parameters used in these calculations based on the values given by Afonso and Ranalli (2004). For profile C-C' the closest heat flow value is in Gelibolu peninsula about 20 km away; profile D-D' falls exactly between two heat flow values therefore geotherms for both of them are calculated; profile E-E' falls only a few km of the heat flow value; and profile H-H' falls again between two heat flow values therefore two geotherms are calculated (Fig. 10). In the case of profiles D-D' and H-H' it can be seen that the temperature difference at the seismic locking depth between the two heat flow values is in the order of 80–100 °C. This range can also be considered as the uncertainty due to the spacing of the available heat flow measurements.

For the first two profiles in Fig. 10 there is a significant disagreement between geodetic (< 10 km) and seismic locking depths (16–17 km). A likely explanation for this may be the spatially heterogeneous frictional properties at the brittle-ductile transition zone (Jiang and Fialko, 2016). Causes of this heterogeneity may be spatially variable lithology/pore pressure, or mechanical heterogeneity resulting from fault immaturity. Indeed, Perrin et al. (2016) classify the western continuation of the North Anatolian Fault as less mature and therefore more likely to exhibit such heterogeneity. The disagreement is less severe along profile H-H' where this time the geodetic locking depth is a few kilometers deeper than the seismic.

Temperatures at the seismic locking depths for profiles C-C', D-D' and E-E' along the Saros basin are in the range of 440–500 °C which appears contrary to the often cited temperature of 300–350 °C that marks the base of the seismogenic layer in quartz-bearing crust (Sibson,

1984). Profile H-H' within the Sporades basin exhibits a seismic locking depth (~13 km) comparable to the other three profiles, even though temperatures are significantly lower (220–300 °C) and a deepening of the locking depth should have occurred. The small variations in the thickness (13–17 km) of the seismogenic layer along the North Aegean Trough may be attributed to a number of factors such as stress regime, lithology or strain rates. As already mentioned, stress regime appears quite uniform along the northern Aegean and Konstantinou et al. (2016) have classified the principal stress axes of all the nodes in the area to the strike-slip stress regime. Lithological changes in the form of a shift from quartz-bearing rocks to rocks rich in feldspar are also capable of shifting the brittle-ductile boundary to 450 °C in agreement with the aforementioned temperatures. However, it is difficult to invoke lithological changes in the absence of detailed tomographic images of the upper crust that would support such an interpretation. On the other hand, the surface strain field affirms a significant variation in strain rate from 600 nstrain/yr in Saros basin to 50 nstrain/yr or less in the Sporades basin (Kreemer et al., 2004; Müller et al., 2013). The effect of higher strain rates along the Saros basin is that rocks may behave in a brittle manner at temperatures much higher than 300–350 °C. Even though lower temperatures in the Sporades basin should have increased the depth where rocks are brittle, the low strain rates may offset this effect and limit the seismicity to the top 13 km. It is well known that near locking depth is the place where all large strike-slip earthquakes are likely to nucleate, as also exemplified by the nucleation depth (~13 km) of the 2014 Samothraki earthquake. These results therefore have important implications for the seismic hazard in this region and can help towards building rupture simulation scenarios that will produce strong-motion shaking estimates.

6. Conclusions

The main conclusions of this study can be summarized as follows:

1. A total of 2300 earthquakes that occurred along the North Aegean Trough and adjacent areas during 2011–2016 were relocated using arrival times picked from 32 weak- and strong-motion permanent stations and utilizing a minimum 1D velocity model. Absolute epicentral locations are very similar to the routine ones provided by NOA, however, hypocentral depths showed significant differences with NOA hypocenters that seem overestimated by 10 km or more.
2. Accurate relative locations were obtained for 1693 earthquakes delineating the main shear zones along the Saros and Sporades basin, but also a number of smaller faults not included in the GREDASS database. This delineation generally agrees with the orientation of rupture zones of historical earthquakes that occurred along the North Aegean Trough published previously by Papadopoulos et al. (2002). While the main shear zone that traverses Saros basin is optimally oriented relative to the maximum stress axis, the one that bounds the Sporades basin exhibits a large reactivation angle implying the occurrence of low friction coefficient and/or high fluid pressure within the fault core. Smaller normal faults were found to co-exist with the main shear zones with an orientation almost perpendicular to the minimum stress axis as observed in the nearby island of Limnos.
3. Locking depth of the main shear zones, expressed as the 95th percentile of the hypocentral depth distribution, is almost constant between 13 and 17 km throughout the North Aegean Trough. This is at odds with the trend of heat flow that is increasing along the Saros basin and decreasing towards the Sporades basin. This discrepancy can be explained once the strain rates are taken into account that tend to also increase along the Saros basin, thus allowing rocks to fail at higher temperatures, and decrease significantly towards the Sporades basin thus limiting any deepening of the locking depth.

Table 4
Summary of the thermal parameters used for calculating the variation of temperature as a function of depth for the four profiles shown in Fig. 10. These parameters have been adopted from Afonso and Ranalli (2004).

| Upper crust | |
|----------------------|------------------------------|
| Thickness | 15 km |
| Heat production rate | 1.4 $\mu\text{W}/\text{m}^3$ |
| Thermal conductivity | 2.5 W/m/K |
| Lower crust | |
| Thickness | 10 km |
| Heat production rate | 0.4 $\mu\text{W}/\text{m}^3$ |
| Thermal conductivity | 2.1 W/m/K |

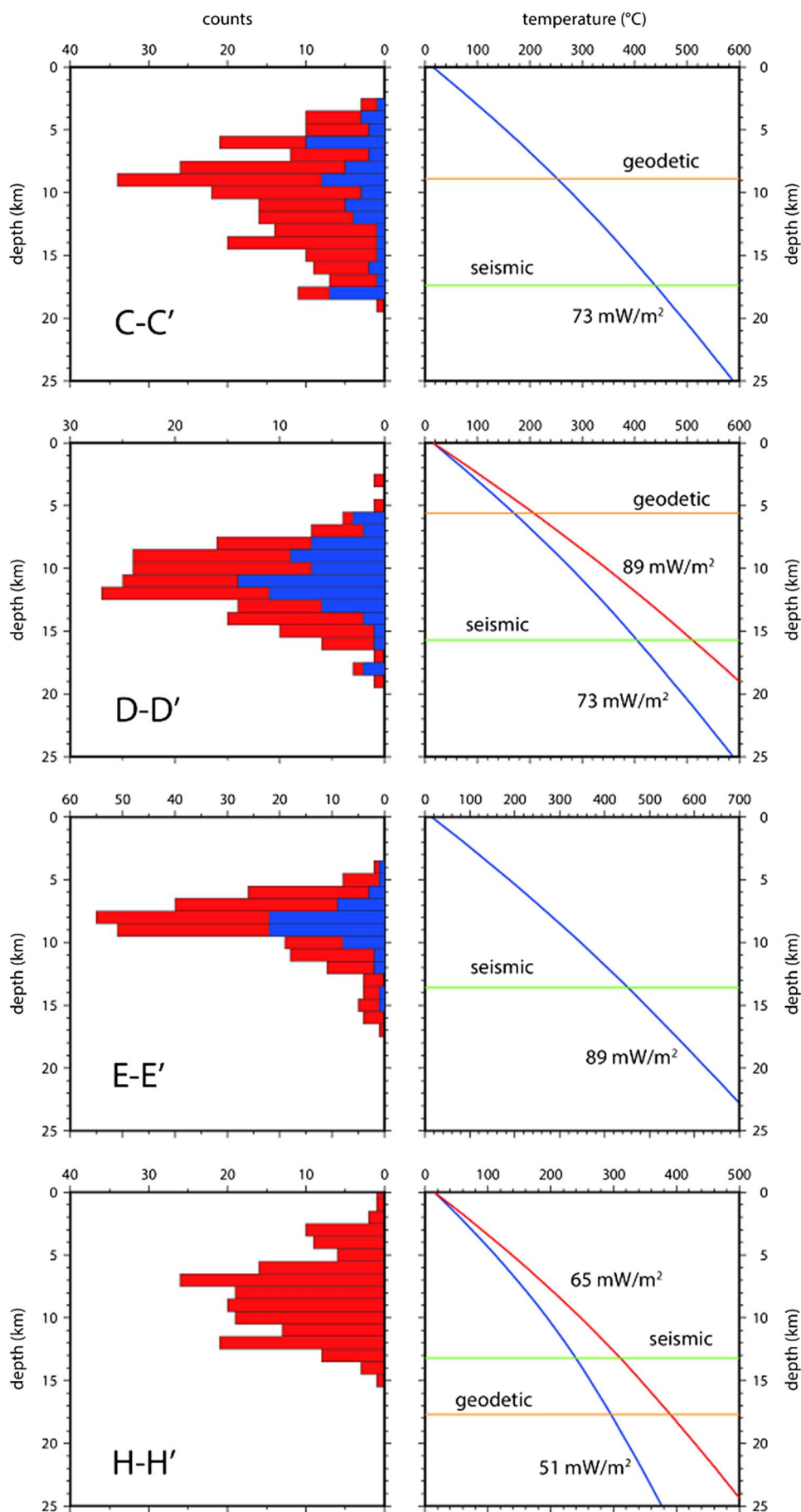


Fig. 10. Histograms that show the hypocentral depth distribution along four profiles shown in Fig. 6 along with calculated temperature as a function of depth (see text for more details). Red bars correspond to distributions calculated using all events while blue bars represent distributions calculated using only events that occurred prior to the 24 May 2014 earthquake. Horizontal lines signify seismic locking depths estimated in this study versus geodetic locking depths adopted from Müller et al. (2013). (For interpretation of the references to color in this figure legend, the reader is referred to the web version of this article.)

Acknowledgments

I would like to thank the Ministry Of Science and Technology (MOST) 105-2116-M-008-005 of Taiwan for the financial support of this research. I would also like to thank the staff of the National Observatory of Athens, Institute of Geodynamics, for their efforts in phase picking and archiving the data. The Co-Editor-in-Chief Kelin Wang and two anonymous reviewers provided helpful comments that improved the original manuscript.

References

- Afonso, J.C., Ranalli, G., 2004. Crustal and mantle strengths in continental lithosphere: is the jelly sandwich model obsolete? *Tectonophysics* 394, 221–232. <http://dx.doi.org/10.1016/j.tecto.2004.08.006>.
- Beniest, A., Brun, J.P., Gorini, C., Grombez, V., Deschamps, R., Hamon, Y., Smit, J., 2016. Interaction between trench retreat and Anatolian escape as recorded by neogene basins in the northern Aegean Sea. *Mar. Pet. Geol.* 77, 30–42. <http://dx.doi.org/10.1016/j.marpetgeo.2016.05.011>.
- Caputo, R., Pavlides, S., 2013. The Greek Database of Seismogenic Sources (GreDaSS), Version 2.0: A Compilation of Potential Seismogenic Sources (Mw > 5.5) in the Aegean Region. <http://gredass.unife.it/http://dx.doi.org/10.15160/unife/gredass/0200>.
- Chatzipetros, A., Kiratzi, A., Zouros, N., Pavlides, S., 2013. Active faulting in the north-eastern Aegean Sea islands. *Tectonophysics* 597–598, 106–122. <http://dx.doi.org/10.1016/j.tecto.2012.11.026>.
- Engdahl, E.R., van der Hilst, R.D., Buland, R.P., 1998. Global teleseismic earthquake relocation with improved travel time and procedures for depth determination. *Bull. Seismol. Soc. Am.* 88, 722–743.
- Evangelidis, C.P., 2015. Imaging supershear rupture for the 2014 Mw 6.9 northern Aegean earthquake by backprojection of strong motion waveforms. *Geophys. Res. Lett.* 42. <http://dx.doi.org/10.1002/2014GL02513>.
- Finzi, Y., Hearn, E.H., Ben-Zion, Y., Lyakhovskiy, V., 2009. Structural properties and deformation patterns of evolving strike-slip faults: numerical simulations incorporating damage rheology. *Pure Appl. Geophys.* 166, 1537–1573. <http://dx.doi.org/10.1007/s00024-009-0522-1>.
- Floyd, M.A., Billiris, H., Paradisis, D., Veis, G., Avallone, A., Briole, P., McClusky, S., Nocquet, J.-M., Palamartchouk, K., Parsons, B., England, P.C., 2010. A new velocity field for Greece: implications for the kinematics and dynamics of the Aegean. *J. Geophys. Res.* 115, B10403. <http://dx.doi.org/10.1029/2009JB007040>.
- Font, Y., Kao, H., Lallemand, S., Liu, C.S., Chiao, L.Y., 2004. Hypocenter determination offshore of eastern Taiwan using the maximum intersection method. *Geophys. J. Int.* 158, 655–675.
- Geiger, L., 1912. Probability method for the determination of earthquake epicenters from the arrival time only. *Bull. St Louis Univ.* 8, 56–71.
- Hollenstein, C., Müller, M.D., Geiger, A., Kahle, H.-G., 2008. Crustal motion and deformation in Greece from a decade of GPS measurements, 1993–2003. *Tectonophysics* 449. <http://dx.doi.org/10.1016/j.tecto.2007.12.006>.
- Jiang, J., Fialko, Y., 2016. Reconciling seismicity and geodetic locking depths on the Anza section of the San Jacinto fault. *Geophys. Res. Lett.* 43. <http://dx.doi.org/10.1002/2016GL071113>.
- Jongsma, D., 1974. Heat flow in the Aegean area. *Geophys. J. R. Astron. Soc.* 37, 337–346.
- Karabulut, H., Roumelioti, Z., Benetatos, C., Mutlu, A.K., Özalaybey, S., Aktar, M., Kiratzi, A., 2006. A source of the 6 July 2003 (Mw 5.7) earthquake sequence in the Gulf of Saros (Northern Aegean Sea): seismological evidence for the western continuation of the Ganos fault. *Tectonophysics* 412, 195–216. <http://dx.doi.org/10.1016/j.tecto.2005.09.009>.
- Kiratzi, A., 2002. Stress tensor inversions along the westernmost North Anatolian Fault Zone and its continuation into the North Aegean Sea. *Geophys. J. Int.* 151, 360–376.
- Kiratzi, A., Tsakirovdi, E., Benetatos, C., Karakaisis, G., 2016. The 24 May 2014 (Mw 6.8) earthquake (North Aegean Trough): spatiotemporal evolution, source and slip model from teleseismic data. *Phys. Chem. Earth* 95, 85–100. <http://dx.doi.org/10.1016/j.pce.2016.08.003>.
- Konstantinou, K.I., 2014. Moment magnitude-rupture area scaling and stress-drop variations for earthquakes in the Mediterranean region. *Bull. Seismol. Soc. Am.* 104, 2378–2386. <http://dx.doi.org/10.1785/0120140062>.
- Konstantinou, K.I., Melis, N.S., Boukouras, K., 2010. Routine regional moment tensor inversion for earthquakes in the Greece region: the National Observatory of Athens (NOA) database (2001–2006). *Seismol. Res. Lett.* 81, 738–748. <http://dx.doi.org/10.1785/gssrl.81.5.738>.
- Konstantinou, K.I., Mouslopoulou, V., Liang, W.-T., Heidbach, O., Oncken, O., Suppe, J., 2016. Present-day crustal stress field in Greece inferred from regional-scale damped inversion of earthquake focal mechanisms. *J. Geophys. Res. Solid Earth* 121. <http://dx.doi.org/10.1002/2016JB013272>.
- Koukouvelas, I.K., Aydin, A., 2002. Fault structure and related basins of the North Aegean Sea and its surroundings. *Tectonics* 21, 1046. <http://dx.doi.org/10.1029/2001TC901037>.
- Kreemer, C., Chamot-Rooke, N., Le Pichon, X., 2004. Constraints on the evolution and vertical coherency of deformation in the Northern Aegean from a comparison of geodetic, geologic and seismologic data. *Earth Planet. Sci. Lett.* 225, 329–346. <http://dx.doi.org/10.1016/j.epsl.2004.06.018>.
- Laigle, M., Hirm, A., Sachpazi, M., Rousos, N., 2000. North Aegean crustal deformation: an active fault imaged to 10 km depth by reflection seismic data. *Geology* 28, 71–74.
- Lomax, A., Virieux, J., Volant, P., Berge-Thierry, C., 2000. Probabilistic earthquake location in 3D and layered models. In: Thurber, Rabinowitz (Ed.), *Advances in Seismic Event Location*, pp. 101–134.
- Lomax, A., Michelini, A., Curtis, A., 2009. Earthquake location, direct, global-search methods. In: *Complexity in Encyclopedia of Complexity and System Science*, Part 5. Springer, New York, pp. 2449–2473. <http://dx.doi.org/10.1007/978-0-387-30440-3>.
- Maleki, V., Hossein Shomali, Z., Hatami, M.R., Pakzad, M., Lomax, A., 2013. Earthquake relocation in the central Alborz region of Iran using a nonlinear probabilistic method. *J. Seismol.* 17, 615–628. <http://dx.doi.org/10.1007/s10950-012-9342-3>.
- McClusky, et al., 2000. Global positioning system constraints on plate kinematic and dynamics in the Eastern Mediterranean and Caucasus. *J. Geophys. Res.* 105, 5695–5719.
- McNeill, L.C., Mille, A., Minshull, T.A., Bull, J.M., Kenyon, N.H., 2004. Extension of the North Anatolian Fault into the North Aegean Trough: evidence for transtension, strain partitioning, and analogues for Sea of Marmara basin models. *Tectonics* 23, TC2016. <http://dx.doi.org/10.0129/2002TC001490>.
- Meijer, P.T., Wortel, M.J.R., 1997. Present-day dynamics of the Aegean region: a model analysis of the horizontal pattern of stress and deformation. *Tectonics* 16, 879–895.
- Moser, T.J., Van Eck, T., Nolet, G., 1992. Hypocenter determination in strongly heterogeneous earth models using the shortest path method. *J. Geophys. Res.* 97, 6563–6572.
- Müller, M.D., Geiger, A., Kahle, H.-G., Veis, G., Billiris, H., Paradisis, D., Felekis, S., 2013. Velocity and deformation fields in the North Aegean domain, Greece, and implications for fault kinematics, derived from GPS data 1993–2009. *Tectonophysics* 597–598, 34–40. <http://dx.doi.org/10.1016/j.tecto.2012.08.003>.
- Nyst, M., Thatcher, W., 2004. New constraints on the active tectonic deformation of the Aegean. *J. Geophys. Res.* 109, B11406. <http://dx.doi.org/10.1029/2003JB002830>.
- Papadopoulos, G.A., Ganas, A., Plessa, A., 2002. The Skyros earthquake (Mw 6.5) of 26 July 2001 and precursory seismicity in the North Aegean Sea. *Bull. Seismol. Soc. Am.* 92, 1141–1145.
- Papanikolaou, D., Alexandri, M., Nomikou, P., Ballas, D., 2002. Morphotectonic structure of the western part of the North Aegean Basin based on swath bathymetry. *Mar. Geol.* 190, 465–492.
- Papazachos, B.C., Papazachou, K., 2003. *The Earthquakes of Greece*. Ziti editions, Thessaloniki.
- Pavlides, S.B., Tranos, M.D., 1991. Structural characteristics of two strong earthquakes in the north Aegean: Ierissos (1932) and Agios Efstratios (1968). *J. Struct. Geol.* 13, 205–214.
- Perrin, C., Manighetti, I., Ampuero, J.-P., Cappa, F., Gaudemer, Y., 2016. Location of largest earthquake slip and fast rupture controlled by along-strike change in fault structural maturity due to fault growth. *J. Geophys. Res. Solid Earth* 121, 3666–3685. <http://dx.doi.org/10.1002/2015JB12671>.
- Pfister, M., Rybach, L., Simsek, S., 1998. Geothermal reconnaissance of the Marmara Sea region (NW Turkey): surface heat flow density in an area of active continental extension. *Tectonophysics* 291, 77–89.
- Podvin, P., Lecomte, I., 1991. Finite difference computation of traveltimes in very contrasted velocity models: a massively parallel approach and its associated tools. *Geophys. J. Int.* 105, 271–284.
- Reilinger, R., McClusky, S., Paradisis, D., Ergintav, S., Vernant, P., 2010. Geodetic constraints on the tectonic evolution of the Aegean region and strain accumulation along the Hellenic subduction zone. *Tectonophysics* 488, 22–30. <http://dx.doi.org/10.1016/j.tecto.2009.05.027>.
- Roumelioti, Z., Kiratzi, A., Melis, N., 2003. Relocation of the 26 July 2001 Skyros island (Greece) earthquake sequence using the double-difference technique. *Phys. Earth Planet. Inter.* 138, 231–239.
- Saatçilar, R., Ergintav, S., Demirbag, E., Inan, S., 1999. Character of active faulting in the north Aegean Sea. *Mar. Geol.* 160, 339–353.
- Saltogiani, V., Gianniou, M., Taymaz, T., Yolsal-Cevikbilen, S., Stiros, S., 2015. Fault slip source models for the 2014 Mw 6.9 Samothraki-Gökçeada earthquake (North Aegean Trough) combining geodetic and seismological observations. *J. Geophys. Res. Solid Earth* 120, 8610–8622. <http://dx.doi.org/10.1002/2015JB012052>.
- Sibson, R.H., 1984. Roughness at the base of the seismogenic zone: contributing factors. *J. Geophys. Res.* 89, 5791–5799.
- Sibson, R.H., 1990. Rupture nucleation on unfavorably oriented faults. *Bull. Seismol. Soc. Am.* 80, 1580–1604.
- Sodoudi, F., Kind, R., Hatzfeld, D., Priestley, K., Hanka, W., Wylegalla, K., Stavrakakis, G., Vafidis, A., Harjes, H.-P., Bohnhoff, M., 2006. Lithospheric structure of the Aegean obtained from P and S receiver functions. *J. Geophys. Res.* 111, B12307. <http://dx.doi.org/10.1029/2005JB003932>.
- Tarantola, A., Valette, B., 1982. Inverse problems = quest for information. *J. Geophys.* 50, 159–170.
- Taymaz, T., Jackson, J., McKenzie, D., 1991. Active tectonics of the north and central Aegean Sea. *Geophys. J. Int.* 106, 433–490.
- Tembe, S., Lockner, D., Wong, T.-F., 2009. Constraints on the stress state of the San Andreas fault with analysis based on core and cuttings from the San Andreas Observatory at Depth (SAFOD) drilling phases 1 and 2. *J. Geophys. Res.* 114, B11401. <http://dx.doi.org/10.1029/2008JB005883>.
- Ustaömer, T., Gökasan, E., Tur, H., Görüm, T., Batuk, F.G., Kalafat, D., Alp, H., Ecevitoglu, B., Birkan, H., 2008. Faulting, mass-wasting and deposition in an active dextral shear zone, the Gulf of Saros and the NE Aegean Sea, NW Turkey. *Geo-Mar. Lett.* 28, 171–193. <http://dx.doi.org/10.1007/s00367-0099-6>.
- Vernant, P., 2015. What can we learn from 20 years of interseismic GPS measurements across strike-slip faults? *Tectonophysics* 644–645, 22–39. <http://dx.doi.org/10.1016/j.tecto.2015.01.013>.
- Waldhauser, F., 2001. HypoDD: a program to compute double-difference hypocentre locations. In: U. S. Geological Survey, Open File Report 01-113.
- Waldhauser, F., Ellsworth, W.L., 2000. A double-difference earthquake location algorithm: method and application to the northern Hayward fault, California. *Bull. Seismol. Soc. Am.* 90 (6), 1353–1368.